Graphene and 2D Materials (2023) 8:161–178
https://doi.org/10.1007/s41127-023-00066-2

ORIGINAL ARTICLE

Mechanical properties of graphene-based gyroidal sheet/shell architected lattices

Somayya E. Taher[1,3] · Juveiriah M. Ashraf[4] · Kin Liao[1,3] · Rashid K. Abu Al-Rub[1,2]

Received: 22 June 2023 / Revised: 27 September 2023 / Accepted: 4 October 2023 / Published online: 19 October 2023

Abstract

Creating 3D cellular structures out of 2D nanomaterials such as graphene is an active area of research since most realistic applications require multi-functional 3D objects. Graphene aerogels that are taking the topology of stochastic foam microstructures have been extensively studied. Additive manufacturing has shifted the focus from stochastic aerogels to architected 3D graphene lattices (3DGL). In this paper and for the first time, we synthesized, characterized, and mechanically tested 3DGLs with microstructures taking the topology of shell-based gyroid structure and compared their properties to tubular 3DGL. 3DGLs were fabricated using a hydrothermal-assisted dip-coating method based on 3D-printed polymer templates. Effects of number of unit cell, graphene oxide (GO) concentration, and polymer template volume fraction have been investigated. It was found that smaller **polymer** template volume fraction, smaller unit cell, and larger GO concentration lead to increased mechanical properties. It was found that the mechanical properties of the synthesized gyroid shell-based 3DGLs outperformed tubular and 3DGLs and stochastic graphene aerogels. Furthermore, both gyroidal shell and tubular 3DGLs exhibit stretching-dominated behavior making them ideal for synthesizing stiffer and stronger graphene lattices. This study serves as a guideline for designing multi-functional shell-based lattices made of 2D materials with enhanced mechanical properties for various applications.

Keywords Graphene · Lattices · 3D printing · Triply periodic minimal surfaces · Template-assisted

1 Introduction

Two-dimensional materials such as graphene [1] and MXenes [2] have seen enormous research interest in the past decade owing to their extraordinary mechanical, thermal, and electrical properties [2, 3]. Extensive studies have shown that graphene has the potential to revolutionize the existing technologies in an unprecedented manner [4]. However, graphene needs tailoring to become readily usable in three-dimensional (3D) applications [5]. Therefore, several techniques have been developed to tailor 2D materials into 3D ones in order to make the most of the exceptional properties offered by the base 2D materials like graphene. An excellent review on the synthesis techniques of 3D graphene aerogels is provided by Sun et al. [6]. In addition, several fabrication methods have been employed to produce graphene foams [7], graphene aerogels [8], and graphene hybrid 3D networks [9–11]. One obvious disadvantage of these fabrication methods lies in the fact that the generated graphene structures are purely stochastic porous networks, thus limiting their functionality when compared to engineered graphene architectures [12].

Recent research focus has shifted toward utilizing architected graphene materials or metamaterials and structures [13, 14]. Several potential candidate lattice architectures can be investigated to improve the physical and mechanical properties of 3D graphene cellular structures. For example, the mathematically known triply periodic minimal surfaces

✉ Rashid K. Abu Al-Rub
rashid.abualrub@ku.ac.ae; rashedkamel@yahoo.com

1 Advanced Digital and Additive Manufacturing Center, Khalifa University of Science and Technology, Po Box 127788, Abu Dhabi, UAE

2 Mechanical and Nuclear Engineering Department, Khalifa University of Science and Technology, Po Box 127788, Abu Dhabi, UAE

3 Aerospace Engineering Department, Khalifa University of Science and Technology, Po Box 127788, Abu Dhabi, UAE

4 Advanced Materials Research Center, Technology Innovation Institute, Abu Dhabi, UAE

(TPMS) have fascinating topologies that provide excellent physical and mechanical properties when utilized as lattices or metamaterials [15]. TPMS were used to design and fabricate architected cellular structures in a wide range of applications, such as catalytic substrates [16], feed-spacers [17], bio-scaffold [18, 19], and thermal management and energy storage [20, 21]. TPMS structures have shown superior performance in these applications compared to conventional lattices. TPMS has a zero-mean curvature at every point on the surface, non-self-intersecting, smooth, and interconnected in the 3D space. TPMS can be either thickened to produce sheet/shell networks, or one of the volumes separated by the surface can be filled to produce solid/ligament/strut networks [22]. Schwarz [23] reported earlier TPMS surfaces, i.e., primitive and diamond. Later, Schoen [24] worked extensively on TPMS surfaces discovering many other TPMS topologies, with the most famous one known as the gyroid.

Generally, when these architected lattices are subjected to a macroscopic loading, their deformation behavior can be classified as bending-dominated, stretching-dominated, or a mix of bending and stretching [25]. Al-Ketan et al. [26] experimentally concluded that sheet-based TPMS cellular materials exhibited a near stretching-dominated deformation behavior, whereas ligament-based TPMS showed a bending-dominated behavior.

In fact, few recent works have highlighted synthesizing 3D graphene structures with TPMS or TPMS-like lattice topologies. Garcia et al. [27] reported a scalable synthesis method using a porous Ni template for chemical vapor deposition (CVD) to fabricate a gyroid-inspired 3D graphene structure with tunable, uniform, co-continuous microstructures with a high Young's modulus of 30 MPa. Hensleigh et al. [28] used the micro-stereolithography additive manufacturing (AM) technique to fabricate complex micro-architected graphene structures based on octet-truss lattice having an approximated gyroid structure within its struts. The fabricated graphene structure exhibits a stretching-dominated behavior. Cebo et al. [29] used CVD and 3D Ni templating of self-assembled voided triblock terpolymer to fabricate free-standing gyroidal graphene tube networks of sub-60 nm unit cell sizes. Similarly, Kashani et al. [30] used CVD and nanoporous Ni template to produce large-scale ultralight nanoporous graphene with a 3D bi-continuous nanoarchitecture approximating the tube-network gyroidal topology. The obtained 3D graphene structure exhibits Young's modulus of 3.8 to 6.6 MPa. Ashraf et al. [31, 32] have developed a simple method to fabricate 3D graphene structures based on 3D-printed polymer templates using a hydrothermal-assisted dip-coating method and applied the method for fabricating tube-ligament networks (i.e., *tubular*) gyroidal graphene lattices. This scalable fabrication technique enables the fabrication of any designed 3D topologies out of 2D nanomaterials. In fact, Fu et al. [33] applied the same approach to fabricate tube-ligament networks gyroidal lattices out of MXene 2D material.

In this regard, this study focuses on fabricating *sheet/shell*-based gyroidal TPMS graphene lattices using the hydrothermal-assisted dip-coating method developed in [32] with modified synthesis parameters and compare their properties to tubular counterparts in our previous work [31, 32], which to the authors' best knowledge has not been done before. For that purpose, we additively manufacture, synthesize, and mechanically test gyroidal TPMS graphene metamaterials based on both the sheet- and tube-ligament networks. The uniaxial compressive mechanical properties of the 3DGL for the sheet- and tube-ligament networks are obtained, where the effects of the network-type (i.e., shell vs tube), unit cell size, template's relative density, and graphene oxide concentration on the mechanical properties are thoroughly assessed. It was found that the mechanical properties of the synthesized gyroid shell-based 3DGLs outperformed both the tubular 3DGLs and stochastic graphene aerogels.

2 Materials and methods

In this section, the methodology adopted for performing the study reported is explained. This includes the design and fabrication of lattices as well as the material characterization and mechanical testing for property evaluation.

2.1 Gyroid ligament- and sheet-lattice topology design

The TPMS gyroid ligament and sheet networks were designed via the MSLattice in-house software [34] (see Fig. 1a). Gyroid is defined mathematically using the following level-set equation:

$$\sin x\cos y + \sin y\cos z + \sin z\cos x = c \tag{1}$$

where $x = 2\pi X/l$, $y = 2\pi Y/l$, and $z = 2\pi Z/l$ with X, Y, and Z as the Cartesian coordinates, l as the size of the unit cell, and c as the level-set constant. For gyroidal solid/ligament networks, a value of $c \leq 0$ solidifies one of the two volumes separated by the iso-surface ($c=0$), whereas a value of $c \geq 0$ solidifies the other volume; thus, c controls the volume fraction of the lattice (or equivalently, the relative density (RD) of the lattice, which is the density ratio of the cellular material to that of the base material). For gyroidal sheet networks, the volume fraction or RD is increased by thickening the iso-surface, such that both void subdomains are equal in volume (see Fig. 1a).

One important parameter of porous structures is the surface area-to-volume (SAV) ratio. Generally, a larger SAV

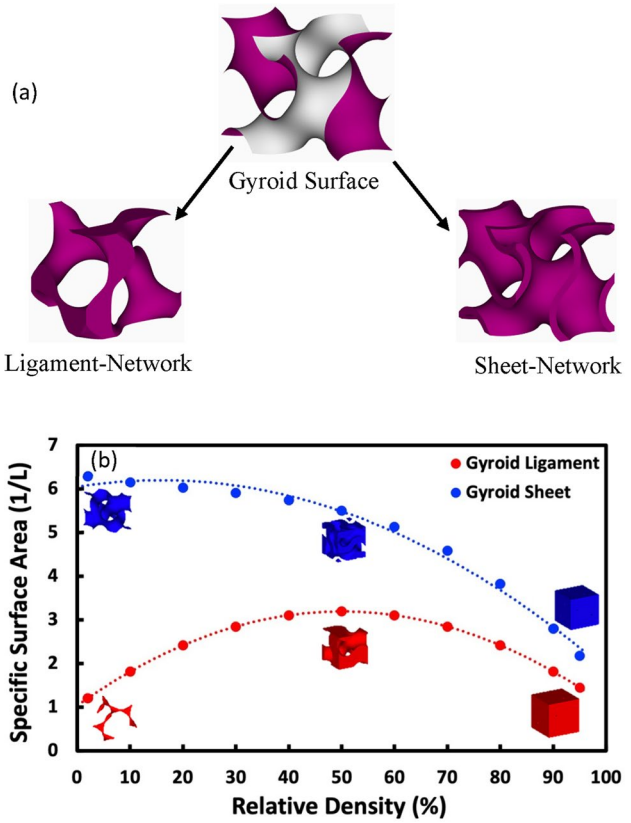

Fig. 1 **a** Unit cells of cellular structures based on the gyroid surface showing the iso-surface, ligament- and sheet-based one unit cell lattice. **b** The surface area-to-volume (SAV) ratio as a function of relative density for gyroid ligament and sheet networks

ratio results in greater heat transfer [15]. Figure 1b shows the variation of SAV ratio (per unit size L) with RD of gyroid ligament and sheet networks. The sheet-based lattices have higher SAV ratio compared to the ligament-based networks at the same relative density. Also, the sheet networks have a higher SAV ratio at low RDs and decreases with increasing RD. While for the ligament network, SAV ratio increases with increasing RD until it reaches a maximum value at RD = 50%, after which it starts decreasing. In this work, gyroidal ligament and sheet network cube templates of 20% RD were generated for 5 × 5 × 5, 10 × 10 × 10, and 15 × 5 × 15 unit cell lattices. The size of the 3D-printed cubic samples was 20 mm with a unit cell size of 4, 2, and 1.333 mm for the 5, 10, and 15 unit cell tessellations. Additionally, gyroidal sheet network templates with 5 × 5 × 5 unit cell were also designed to study the effect of two different polymer template RDs (7% and 20%) on mechanical properties.

2.2 Experimental synthesis

The polymer templates of gyroid ligament and sheet networks of 7 and 20% relative density were additively manufactured using the Formlabs (Boston, MA, USA) (Form2) stereolithography (SLA) 3D printer with a layer thickness resolution of 100 µm. The Formlabs SLA technique is based on solidifying a photopolymer resin with each layer being exposed to a 405-nm blue laser with a spot size of 140 microns and power of 250 mW. The liquid resin employed in this work was the Formlabs Castable Wax Resin with 20% wax fill. In post-printing, the samples were washed in isopropyl alcohol (IPA) to remove any residual polymer on the surface of the 3D-printed lattices. Four replicates of each lattice type were fabricated for mechanical properties measurements.

To fabricate the free-standing gyroidal graphene lattices, a combination of template-assisted method and hydrothermal-assembly and subsequent thermal etching of the polymer scaffolds was employed, following the synthesis technique in [31]. In this method, graphene oxide (GO) solution (Graphenea Inc., Spain) of different concentrations (2, 4, 10, and 15 mg/mL) was coated onto the 3D-printed lattice polymer templates under hydrothermal conditions, after which the polymer template was removed via direct sublimation at elevated temperatures. The GO was chemically reduced to rGO by hydrazine hydrate (Sigma-Aldrich, USA) via elimination of the excess oxygen-functional groups in the GO, causing an increase in the π–π conjugated bonds of rGO. Here, we briefly describe the synthesis process which is schematically depicted in Fig. 2. To start, 15 mL of the GO dispersion and 2.5 v/v% of the hydrazine hydrate solution (64% concentration) were mixed. The solution was stirred at room temperature for 5 min at 300 rpm to achieve a homogenous mixture. The 3D-printed lattices were then placed in the prepared mixture and ultra-sonicated for 1 h. Finally, the GO/hydrazine hydrate mixture and the 3D-printed scaffold were transferred to an autoclave (TOPTION, Shaanxi, China) and hydrothermally treated for 6 h at 120 °C, which resulted in the rGO-coated polymer scaffolds. These were rinsed with deionized water several times to wash out any traces of hydrazine and then dried for 24 h at 60 °C. Lastly, the samples were thermally etched for 1.5 h at 400 °C with a heating rate of 1 °C/min in a tube furnace (MTI Corporation Company, USA) to remove the polymer scaffold and obtain free-standing 3D graphene lattices (3DGL). The 3D graphene lattice based on tube-ligament and sheet networks is labeled 3DGL-T and 3DGL-S, respectively, throughout the paper.

After fabrication, the dimensions of the 3DGL were measured, that were approximately 14 mm × 14 mm × 14 mm, resulting in a shrinkage of ~ 30% (based on the length dimensions) with a unit cell size of 2.8, 1.4, and 0.9331 mm for the 5, 10, and 15 unit cell tessellations, respectively. To verify the complete removal of the polymer, five samples of the 10 × 10x10 unit cell 3DGL-S with 20% polymer RD were further heat-treated at 400 °C three times with the

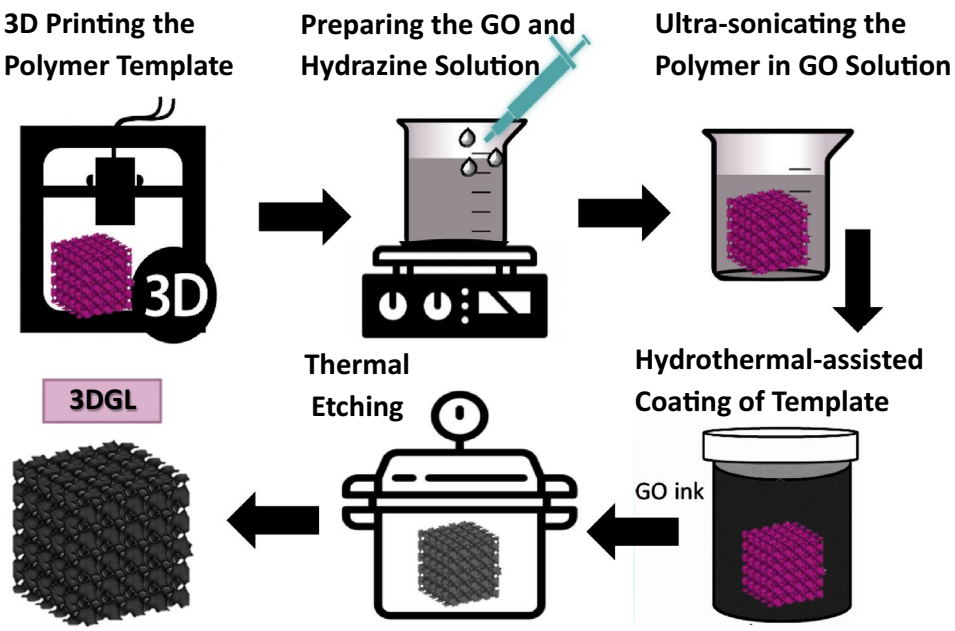

Fig. 2 Schematic of the synthesis process for free-standing 3D graphene lattice (3DGL)

density being measured after each process. It was found that the density of the lattices remained the same: 121.79, 121.26, and 121.21 mg/cm^3 after the first, second, and third thermal etching processes, respectively, thus corroborating the complete removal of the polymer template.

2.3 Microstructural characterization

Scanning electron microscopy (SEM, JEOL, Model JSM-7610F) was used to depict the morphology of the fabricated 3DGL and to measure the thickness of the gyroid sheets. Furthermore, micro-X-ray computed tomography (micro-CT, Phoenix Nanotom) was employed to scan the internal structure of the specimens and to evaluate the volume fraction (or equivalently the relative density) of the graphene in the lattices. ImageJ was then employed on the micro-CT cross-sectional scans to determine the rGO coating layer thickness in the lattices (with an average of 3 measurements taken for each sample), and for measuring the spacing between the rGO sheets after polymer etching. The presence of rGO was confirmed by Raman spectroscopy (WITec alpha300 RAS), while the crystallinity of the rGO base material was verified by X-ray diffraction (XRD Bruker D2 phaser). Thermogravimetric (TGA) analysis was carried out via the TA Instruments SDT 650 Simultaneous Thermal Analyzer to investigate the amount of residual polymer in the graphene gyroid specimens after etching the 3D-printed templates. TGA tests were done for the rGO sheets (of initial 4 and 15 mg/mL concentrations) with a heating profile like the one employed in the thermal etching process, i.e., 25–500 °C at a heating rate of 1 °C min^{-1}. Moreover, since the 3D printing resin used was the same as studied in [31], the TGA data were obtained from the aforementioned work. Nanoindentation by the atomic force microscope (AFM, Asylum Research) was employed [35] to measure the elastic modulus of the synthesized rGO sheets following the procedure in [36]. The AFM with a diamond cube corner tip on a silicon cantilever was operated in a tapping mode (AC-mode) with a drive frequency of 270.376 kHz close to its resonant frequency of 300 kHz. The rGO sheets were placed onto a glass substrate and nine measurements in a square grid have been taken for three samples to obtain an average elastic modulus.

2.4 Mechanical testing

Quasi-static uniaxial compression testing was performed using the Instron 5940 (Instron, Norwood, Massachusetts, USA) equipment under 0.005 mm/s displacement-controlled rate and using a 2 kN load cell. The samples were positioned carefully in the center of the smooth parallel compression plates to ensure uniform loading, reduce friction, and eliminate any undue moments induced by specimens' eccentricity. The test was stopped when the densification of the sample was reached. Four sample replicates of each case have been tested. The following mechanical properties are extracted from the stress–strain diagrams: (1) The elastic modulus was determined by obtaining the maximum slope of linear part of the stress–strain diagram before yielding, (2) plateau strength was calculated by taking the average flow stress for the strain values between 20 and 50%, and (3) the toughness (or energy absorption) was obtained as the area under the stress–strain curve up to 70% strain.

The theoretical values for topological stiffness and strength of isotropic cellular structures are bounded by Hashin–Shtrikman (HS) and Suquet upper bounds [37]. The HS and Suquet bounds for a composite material consider the homogenization of voids. The upper bound of HS and Suquet for the effective elastic modulus (E_{HSU}) and strength ($\sigma_{y,SU}$), respectively, of isotropic materials can be determined using the following equations:

$$\frac{E_{\mathrm{HSU}}}{E_s} = \frac{2\overline{\rho}(5v-7)}{13\overline{\rho}+12v-2\overline{\rho}v-15\overline{\rho}v^2+15v^2-27} \tag{2}$$

$$\frac{\sigma_{y,SU}}{\sigma_s} = \frac{2\overline{\rho}}{\sqrt{4+\frac{11}{3}(1-\overline{\rho})}} \tag{3}$$

where E_s is the elastic modulus, σ_s is the strength, v is the Poisson's ratio for the base material (rGO), and $\overline{\rho}$ is the relative density of the graphene lattice.

3 Results and discussion

3.1 Microstructural characterization

Figures 3 and 4 illustrate examples of 3D-printed polymeric samples, 3D-printed gyroid after rGO coating, and the free-standing 3D graphene gyroid after the thermal etching process for sheet networks and tube-ligament networks, respectively, with different periodicities of 5×5×5, 10×10×10 , and 15×15×15 unit cell. The SEM images (Fig. 5 (a-f)) showed that the morphology of the gyroid sheet networks was well retained after the GO coating and polymer etching process. A high degree of replication was noticed despite increasing the number of unit cells from 5×5×5 to 10×10×10 and 15×15×15 (a total increase of 27 times), proving the fabrication technique's scalability along with its ability to maintain structural accuracy for up to 3375 unit cell lattices. The thickness of the 3DGL-S was derived from the SEM micrographs which were, on average for 5 measurements each, 59.8 ± 3.68 µm for the 5×5×5 unit cell, 48.3 ± 4.59 µm for the 10×10×10 unit cell and 34.5 ± 3.43 µm for the 15×15×15 unit cell lattices (Fig. 5), justifiably decreasing as the number of unit cells increases since both the lattice dimensions as well as the polymer template's relative density (20% RD) are kept constant, while the surface area increases with increasing number of unit cells. In fact, this relation of decreasing thickness with increasing number of unit cells was also noticed by measuring the thickness of the 3D-printed gyroid polymer templates at 20% RD, which showed a value of 0.26 mm for the 5×5×5 unit cell and 0.15 mm for the 10×10×10 unit cell sheet networks (see Figure S1 of the supplementary document). The rGO sheet thickness was also determined for 5×5×5 unit cell lattice of 7% polymer RD and was found

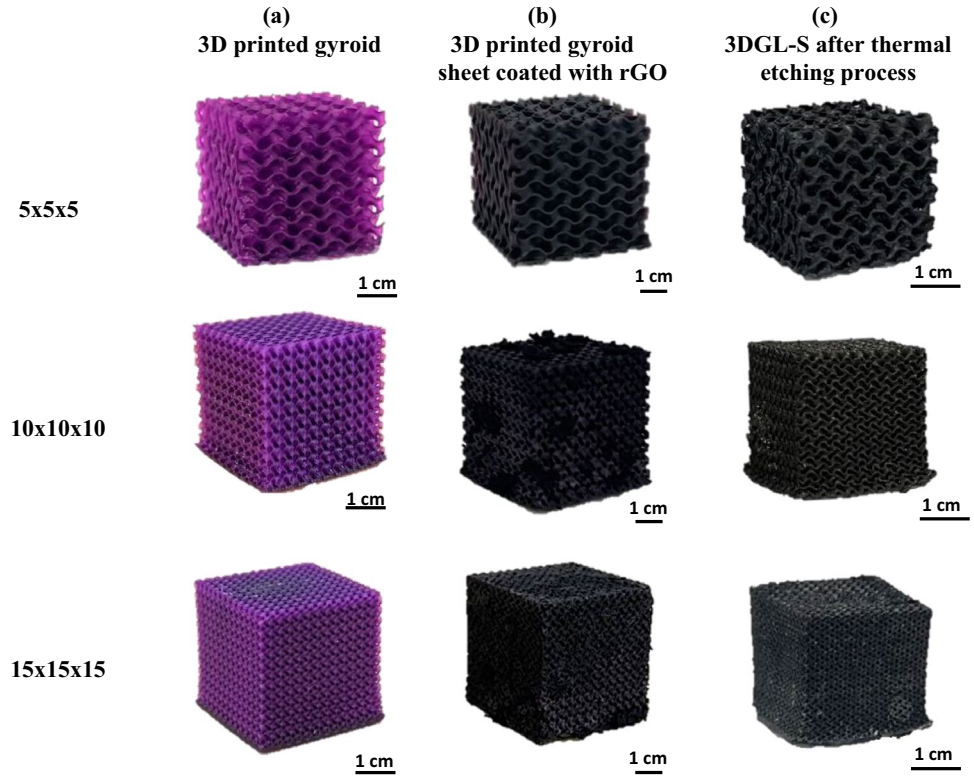

Fig. 3 Illustrations of sample images for 5×5x5, 10×10x10 and 15×15x15 unit cell **a** 3D-printed gyroid sheet-network lattices, **b** 3D-printed gyroid sheet networks coated with rGO (4 mg/mL GO concentration) after the hydrothermal process, and **c** free-standing 3DGL-S after the thermal etching process

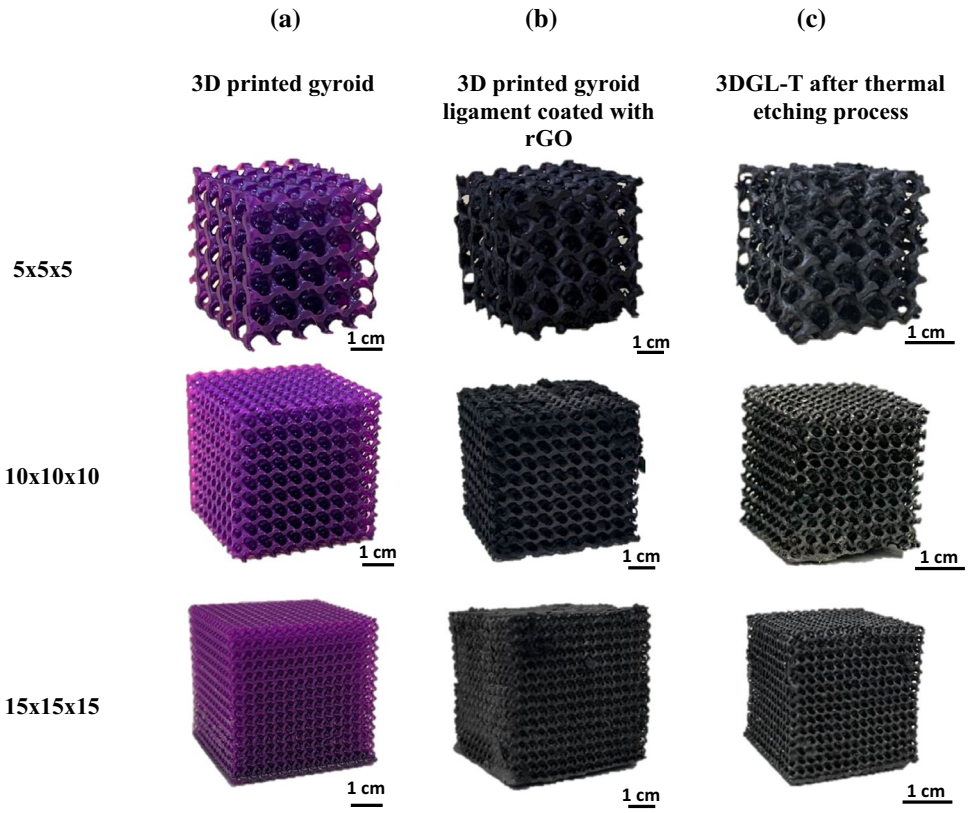

Fig. 4 Illustrations of sample images for 5 × 5x5, 10 × 10x10 and 15 × 15x15 unit cell **a** 3D-printed gyroid ligament-network lattices, **b** 3D-printed gyroid ligament networks coated with rGO (4 mg/mL GO concentration) after the hydrothermal process, and **c** free-standing 3DGL-T after the thermal etching process

to be approximately 28 µm (see Figure S2(a) of the supplementary document).

Micro-CT layer-by-layer scans revealed near-hollow 3DGL-S when using a sheet-network polymer template (Fig. 6d–f) and hollow/tubular ligaments when using a ligament-network polymer template (Fig. 7b), demonstrating the successful polymer removal from the gyroid lattices and further reinforcing synthesis precision as a fair comparison was established between the micro-CT slices and the CAD cross sections of the gyroid sheet networks (see Fig. 6a–c). Figure 6g–i shows the 3D volume rendering of the micro-CT scanning indicating very good preservation of designed lattice topology. The graphene volume fraction in the fabricated lattices (i.e., the solid volume divided by the total volume or equivalently the relative density) was obtained from the micro-CT scans. It was found that in both, the 3DGL-T and 3DGL-S for 5 × 5 × 5, 10 × 10 × 10, and 15 × 15 × 15 unit cell lattices, the graphene volume fraction is increasing as the number of unit cells increases (5.91, 7.61, and 9.83% for 3DGL-T, and 6.19, 10.94, and 15.22% for 3DGL-S) for 20% polymer RD and a 4 mg/mL GO concentration (see Table S1 of the supplementary document). Furthermore, increasing the GO concentration from 2 to 4, 10 and 15 mg/mL increased the graphene volume fraction in the 3DGL-S from 5.78 to 6.19, 7.14 and 8.18%, respectively (see Table S2 of the supplementary document). A similar trend is noticed for 3DGL-S lattices with polymer template RD of 7%; the graphene volume fraction increases from 5.90 to 8.87% for 2 to 15 mg/mL GO concentrations, respectively (Table S3 of the supplementary document). An interesting observation made here is that the rGO volume fraction surpasses that of the polymer RD (7%) at high GO concentrations (10 and 15 mg/mL), which can be attributed to the formation of much thicker rGO sheets constituting the resulting graphene gyroid lattices. For example, the rGO thickness is around 25 ± 2.00 and 28 ± 1.00 µm for the 2 and 4 mg/mL GO concentrations, respectively, while this increases to 33 ± 1.00 and 38 ± 2.00 µm for 10 and 15 mg/mL, respectively (Figure S3 of the supplementary document). This proves that the fabrication process allows increasing rGO sheet thickness by altering GO concentration, through which the lattices' structure can be tuned to achieve the desired properties. It is imperative to mention here that for both polymer template RDs (7 and 20%), the resulting rGO volume fractions are similar for the corresponding GO concentrations. This finding reiterates the successful sublimation of the polymer resin, which would otherwise show a higher solid volume fraction in the 20% RD lattices in case of larger amounts of polymer residue after thermal etching. On comparing the micro-CT slices for the TPMS lattices with 20% and 7% polymer RDs (Figs. 6d and S2(b), respectively), it is noticed that in the latter structures, the rGO sheets are closer to each

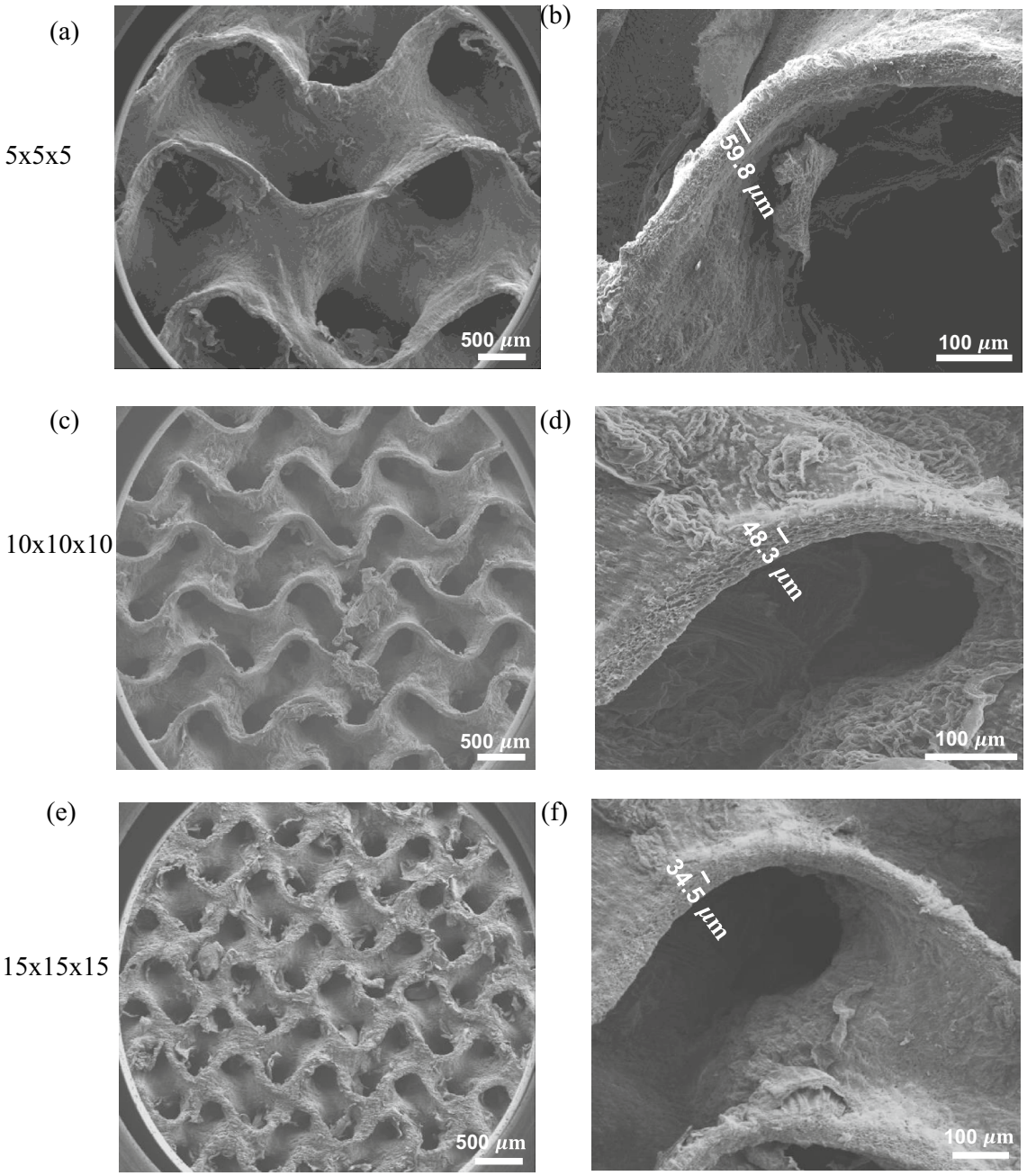

Fig. 5 SEM images of 3DGL-S using GO solution of 4 mg/mL and polymer of 20% RD with **a**–**b** 5×5x5, **c**–**d** 10×10x10, and **e**–**f** 15×15x15 unit cell lattices. Images in the right column shows decreasing sheet thickness as number of unit cells increases

other (approximately 28 ± 2.00 μm or less) compared to the 20% RD (around 111 ± 4.00 μm), allowing the merging of rGO sheets at specific points throughout the network, which may account for the superior mechanical properties of these structures as will be further elaborated in the subsequent sections. On the other hand, Fig. 7 shows the SEM image and micro-CT-scans of the 3DGL-T (15 × 15 × 15 unit cell) with a polymer RD of 20%, with a rGO sheet thickness of 20 ± 1.00 μm. One can notice that gyroid ligament networks are well preserved after the GO coating and polymer etching processes, resulting in hollow tubular 3DGL-Ts with smooth interconnected networks.

XRD peaks revealed the efficient reduction of GO to rGO via hydrazine hydrate for the 3DGL synthesized with all four GO concentrations (i.e., 2, 4, 10, and 15 mg/mL) for 5 × 5 × 5 unit cell, with a prominent peak at $2\theta = 26°$ (Fig. 8a), corresponding to a lattice spacing of 0.34 nm, which is only 1.47% higher than 0.335 nm of graphene's in a single crystal

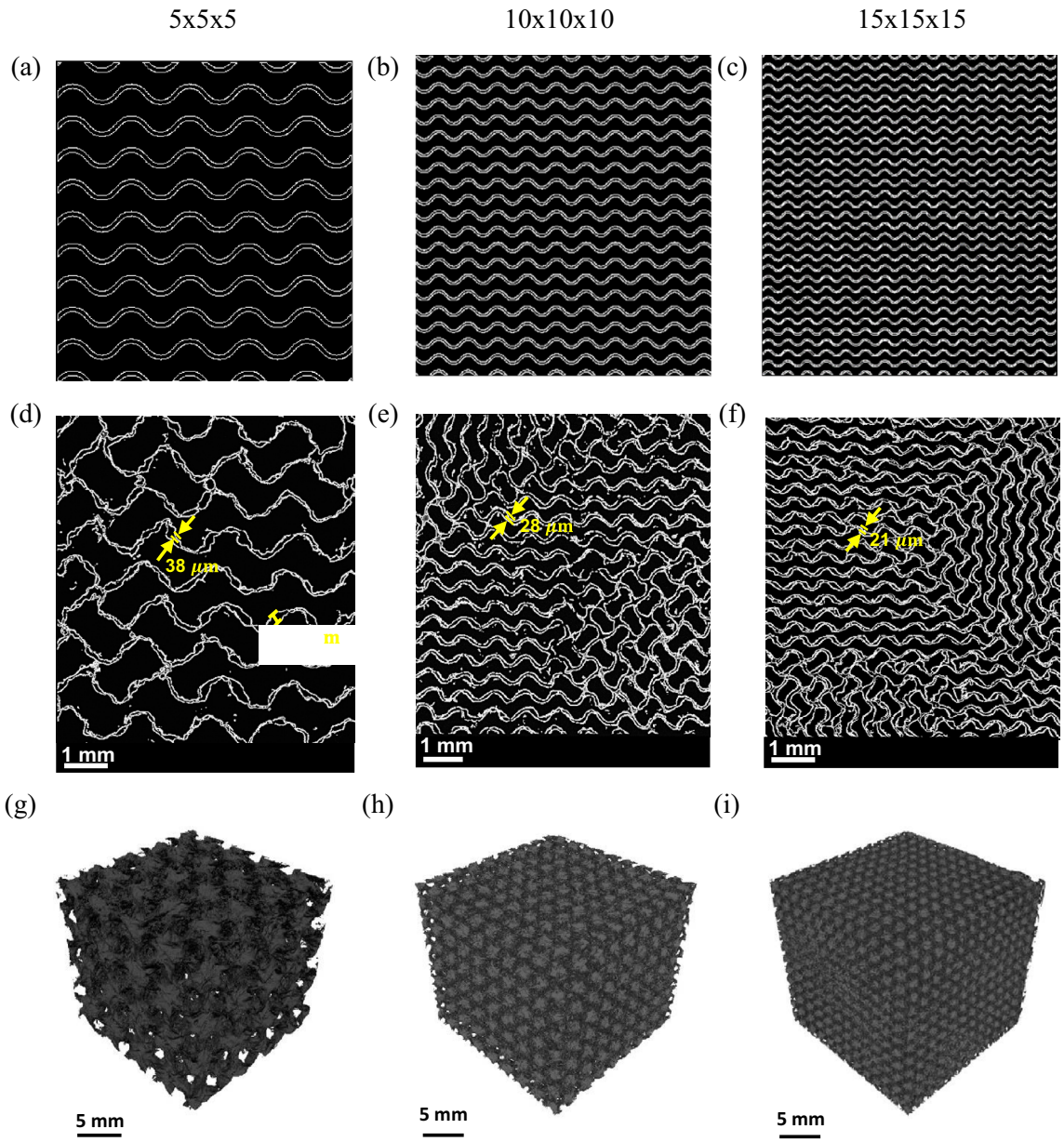

Fig. 6 **a–c** Cross-sectional views generated using CAD, **d–f** micro-CT scans of cross-sectional views, **g–i** 3D view of micro-CT scans of 3DGL-S using 4 mg/mL GO solution concentration and polymer template of 20% RD

natural graphite with ABAB stacking [38], and a (002) diffraction peak [39]. The peaks showed a slight rightward shift with decreasing GO concentration which could be related to increasing number of point defects in rGO flakes as a result of higher oxygen removal sites [40]. The XRD patterns for rGO lattices of $5\times5\times5$ and $10\times10\times10$ unit cell with a GO concentration of 4 mg/mL (Fig. 8b) showed no distinctive differences in the peaks, verifying that the resulting rGO crystallinity via the hydrothermal process is independent of the unit cell size. The same could be said for the polymer template relative density (see Fig. 8a for RD = 7% and Fig. 8b for RD = 20%) that showed no difference in the XRD peaks, proving consistency in the quality of rGO produced.

Raman spectroscopy measurements of the 3DGL-S (Fig. 8c) ensured the quality of rGO was preserved for the lowest and highest concentrations (2 and 15 mg/mL) of the GO solution used in the synthesis process. The customary D and G peaks that are attributed to the sp^3 carbon atoms (K-point phonons) and sp^2-hybridized carbon (E_{2g} phonons), respectively, were recorded for both samples [41]. The G-band is present at a wavenumber of 1583.68 cm^{-1}, corresponding to in-plane vibrations between the carbon

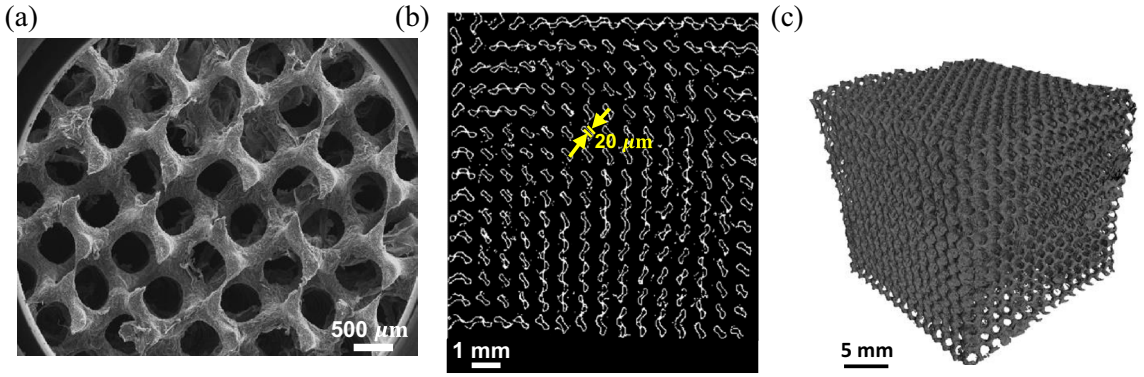

Fig. 7 **a** SEM image, **b** micro-CT-scan of cross-sectional view and **c** 3D view of micro-CT scans of 3DGL-T (15×15x15 unit cell) using 4 mg/mL GO solution concentration and polymer template of 20% RD

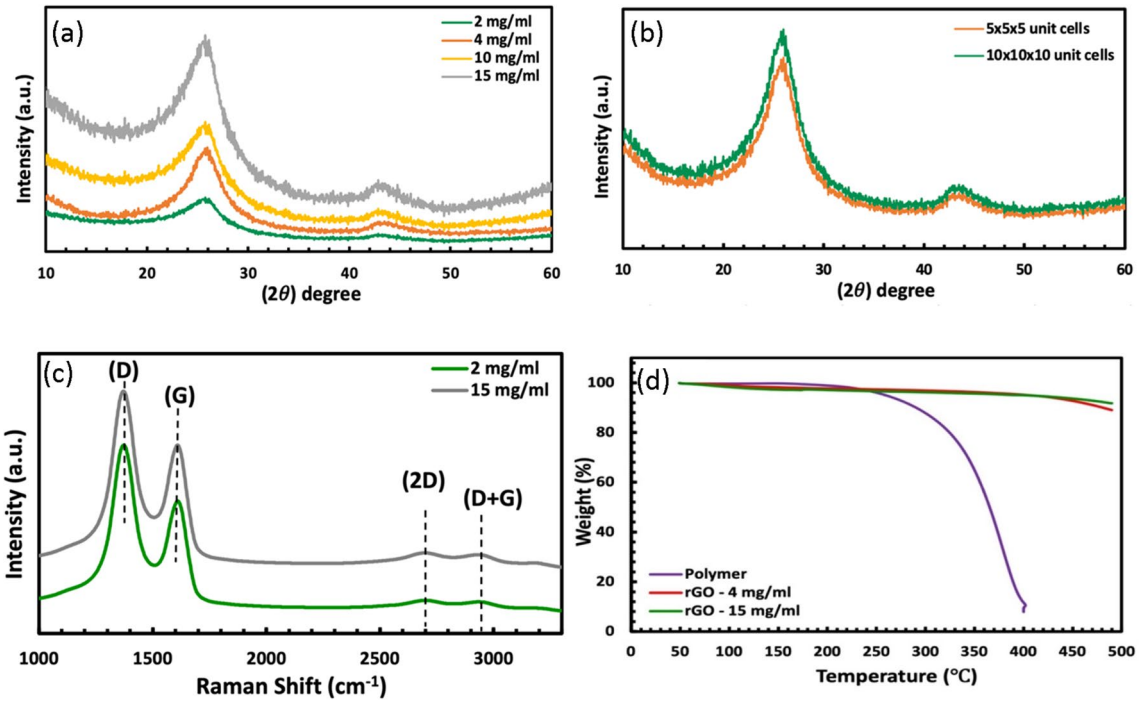

Fig. 8 **a** XRD analysis of 3DGL-S of 5×5x5 unit cell at different GO concentrations with a polymer RD of 7%, **b** XRD analysis of 3DGL-S of 5×5x5 and 10×10x10 unit cell lattices with GO concentration of 4 mg/mL and a polymer RD of 20%, **c** Raman spectra of 3DGL-S with 2 and 15 mg/mL GO concentrations, and **d** TGA results for 3D-printed polymer [31] and 3DGL-S with GO concentrations of 4 and 15 mg/mL

atoms, and a D peak sits at approximately 1342.01 cm^{-1}, relating to the disorder band. The high intensity of the D peak compared to a typical pristine graphene sample in which the D-band is minimum indicates structural defects due to the removal of oxygen-containing functional groups [42]. The curved and disordered domains of the resulting rGO sheets as opposed to a flat, continuous sheet of graphene also contribute to the widened D and G peaks in the 3D graphene networks [29]. The 2D peak (occurring at 2672.06 cm^{-1}), which is sensitive to the π-band in the graphitic electronic structure, is of negligible intensity in the rGO samples, signifying the multi-layered nature of the material. Moreover, a slight D + G band is also observed around a wavenumber of 2916.91 cm^{-1}, which is induced by disorder in the material. The I_D/I_G intensity ratio, according to the Tuinstra–Koenig relation, is used as a measure of defect density. Here, the 3DGLs samples with 2 and 15 mg/mL GO concentrations have a peak intensity ratio of 1.24 and 1.20, respectively, showing a slightly higher number of defects in the sample of lower

concentration due to the larger number of oxygen removal sites.

TGA results (Fig. 8d) confirmed the efficient etching of the polymer scaffolds during the fabrication process which is evident from the low percentage of the material at high temperatures, while the rGO was thermally unreactive, with only 8–12% reduction in the total mass, confirming its excellent thermal stability at temperatures even above 400 °C.

3.2 Mechanical properties

After the design, manufacturing, and characterization of the gyroidal graphene lattices, the mechanical properties' evaluation using uniaxial compression testing was performed to determine the mechanical behavior of optimized 5, 10, and 15 unit cells free-standing 3DGL.

3.2.1 Effect of gyroidal network type: sheet versus tube-ligament networks

A typical stress–strain curve of 3DGL under compression testing can be seen in Figure S4 of the supplementary document for 3DGL based on tube-ligament and sheet networks. Excellent repeatability is shown in Figure S4 when testing two replicates and when even testing four replicates (see Figure S5). It can be readily observed that the 3DGL exhibits a mechanical behavior typical of cellular materials [43]. The stress–strain curve for such materials is usually consist of three regions: the first region is the elastic region under low-stress conditions, the second region is the long collapse plateau, and a region where stress starts to rise dramatically, and the material gets densified under the applied compressive load. For objective comparisons, Fig. 9 shows the normalized (per density) stress–strain responses of 3DGL based on the two different topologies (i.e., tube-ligament and sheet networks) using different periodicities (5, 10, and 15 unit cell) for 20% polymer template RD and 4 mg/mL GO concentration along with their deformation patterns. One

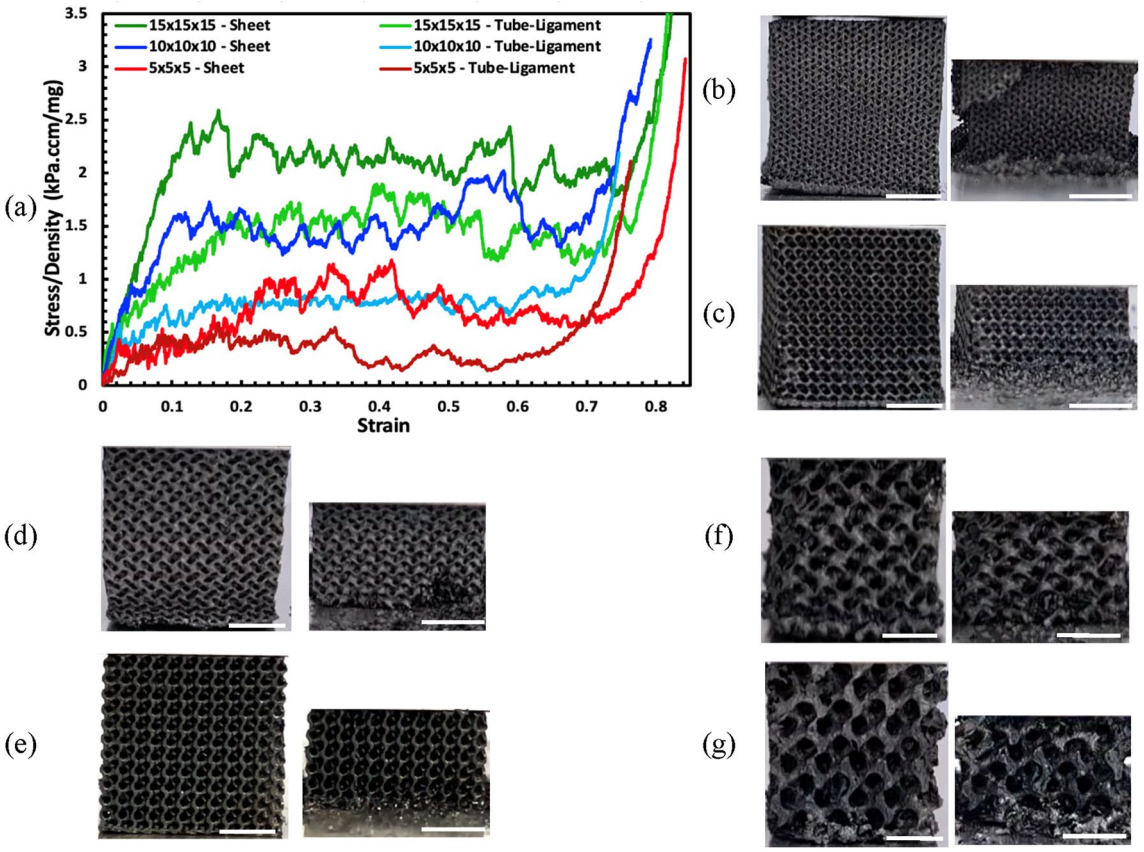

Fig. 9 **a** Comparison of normalized (per density) stress–strain curves of 3DGL-T and 3DGL-S using GO concentration of 4 mg/mL for 20% polymer template RD and 5×5x5, 10×10x10, and 15×15x15 unit cell. Deformation patterns at $\varepsilon = 0\%$ and 50% of 3DGL with polymer RD 20% using GO concentration of 4 mg/mL for **b** 3DGL-S (15×15x15), **c** 3DGL-T (15×15x15), **d** 3DGL-S (10×10x10), **e** 3DGL-T (10×10x10), **f** 3DGL-S (5×5x5), and **g** 3DGL-T (5×5x5), scale bar 1 cm

can notice that the 3DGL samples of the same architecture, the overall mechanical behavior improves with decreasing the unit cells size, while comparing the two topology types, one can notice that sheet networks outperformed the tube-ligament networks.

Table S1 summarizes the extracted compressive mechanical properties and their specific values (i.e., per density) of the 3DGL-T and 3DGL-S for GO concentration of 4 mg/mL using a polymer template of 20% RD. An inspection of Table S1 reveals that 3DGL-S exhibited higher density than the 3DGL-T ones due to the higher surface area of the sheet networks (see Fig. 1b) and, more importantly, offered better mechanical properties. Therefore, at fixed unit cell size, fixed polymer template relative density, and a fixed GO concentration, the sheet networks significantly outperformed tube-ligament networks. For the case of 5 × 5x5 unit cell, Young's modulus, plateau strength, and toughness of sheet configuration were found to be 4.38, 2.73, and 2.85 times higher than that of tube-ligament configuration, respectively. For a more objective comparison, the specific mechanical properties are calculated and listed in Table S1. The specific stiffness, specific plateau strength, and specific toughness are 1.88, 1.49, and 1.6 times higher for sheet networks as compared to the tube-ligament networks. A similar observation can also be made in the case of 10 and 15 unit cells. Hence, network type has a pronounced effect on the measured mechanical properties of 3DGL. Al-Ketan et al. [15] also observed this effect of enhanced mechanical properties under compression testing for metallic TPMS sheet networks. The comparison of sheet- and tube-ligament networks of graphene gyroid lattices is reported herein for the first time in the literature as per the authors' best knowledge.

3.2.1.1 Effect of varying the number of lattice unit cells The focus of this section is on the effect of number of unit cells (or equivalently the effect of unit cell size) on the mechanical properties of 3DGL-S and 3DGL-T, while the size of the cubic samples is fixed. Upon inspection of Table S1, it becomes evident that a higher number of unit cells results in increasing the graphene relative density and enhanced mechanical properties of 3DGL for a fixed value of GO concentration (4 mg/mL) and polymer relative density (RD = 20%). The graphene relative density in 5 × 5 × 5, 10 × 10 × 10, and 15 × 15 × 15 unit cells was 6.19, 10.94, and 15.22%, respectively, as this increase with the increase in number of unit cells can be attributed to the increased surface area. For the case of 5 × 5 × 5 unit cells of 3DGL-S, the values for measured specific stiffness, specific plateau strength, and specific toughness were 11.06, 0.73, and 48.4 kJ.cm^3/mg.m^3, respectively. Upon increasing the number of unit cells to 10 × 10 × 10 of 3DGL-S, the values of measured specific stiffness, specific plateau strength, and specific toughness increased by 1.64, 2.11, and 1.80 times, respectively. Upon further increase in the number of unit cells

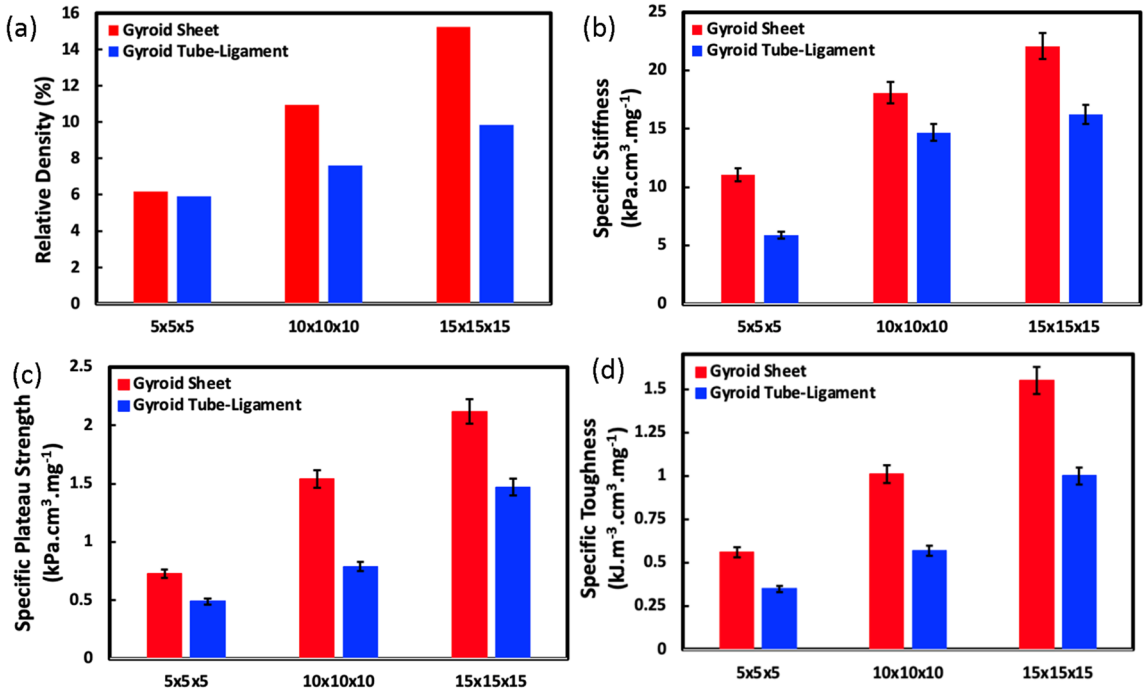

Fig. 10 Effect of number of unit cells for 3DGL-S and 3DGL-T for 4 mg/mL GO concentration and 20% polymer template relative density **a** relative density, **b** specific stiffness, **c** specific plateau strength, and **d** specific toughness for 3D graphene

to 15×15×15 unit cells, the values of measured specific stiffness, specific plateau strength, and specific toughness increased by 2.0, 5.76, and 2.77 times, respectively, than the ones obtained for 5×5×5 unit cells. The same observation can be made in the case of 3DGL-T. Notably, the enhancement owing to the increase in the number of unit cells is more pronounced as compared to the mechanical properties' enhancement effect owing to the network type. To highlight this further, Fig. 10 shows the relative density, specific stiffness, specific plateau strength, and specific toughness of the considered two topologies at the three unit cell tessellations (or equivalently at different unit cell sizes). From Fig. 10, we can clearly see that the 3DGL based on sheet networks always show superior mechanical properties. Also, as the number of unit cells increases (or equivalently as the size of the unit cell decreases), the mechanical properties are increased for both 3DGL-S and 3DGL-T. One expects that with further decrease in the unit cell size, further enhancements are expected in specific mechanical properties. However, we could not explore this further due to the limitations in the SLA 3D printing technique. Micro/nano-3D printing techniques such as two-photon lithography direct laser writing [22] and large-area projection micro-stereolithography [44] can be used to 3D print polymer templates with much smaller unit cell size, but the challenge would be the difficulty of using the current dip-coating.

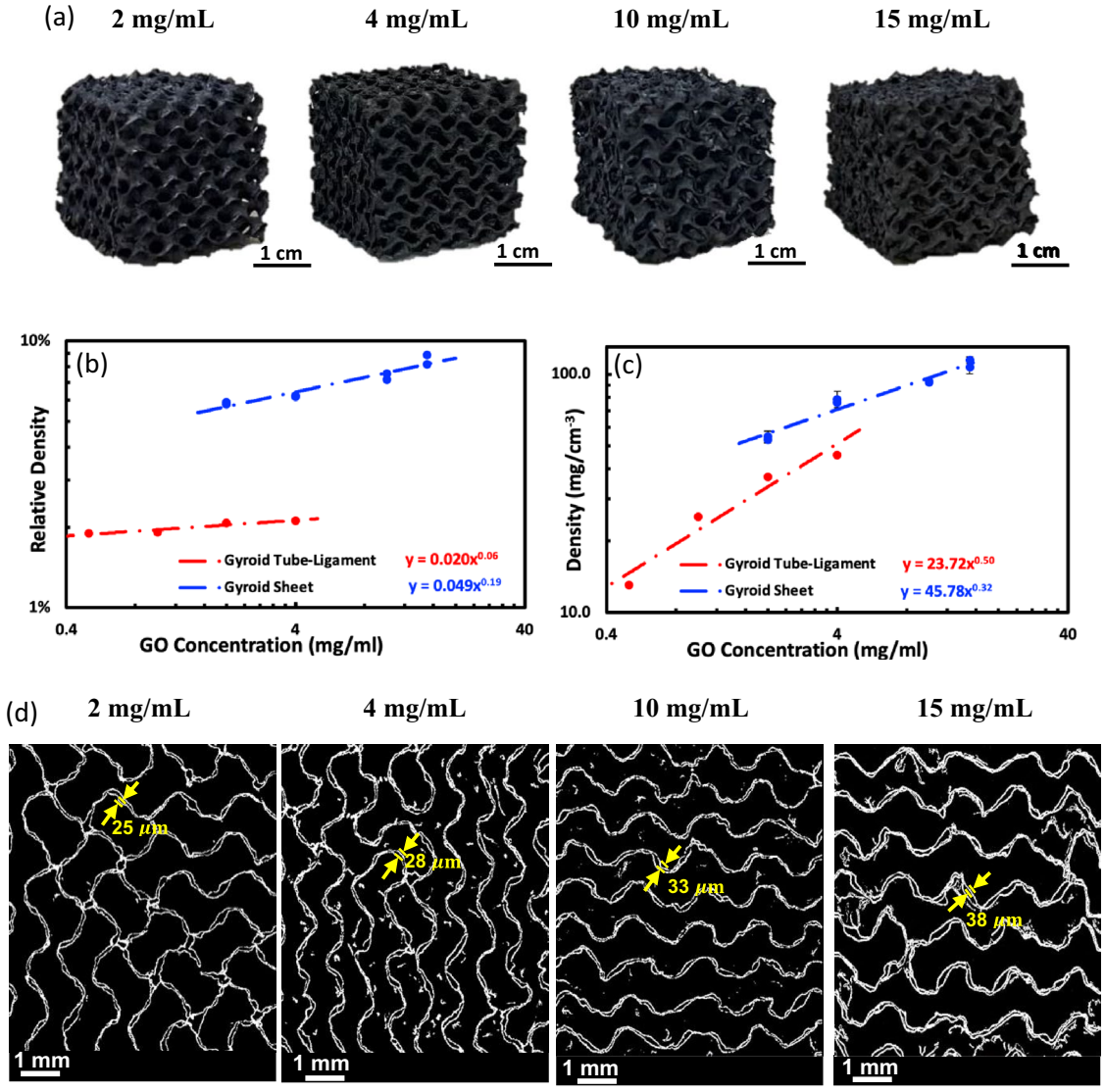

Fig. 11 **a** Optical images of 5×5x5 unit cell 3DGL-S samples for 20% polymer template RD using four GO concentrations, **b** 3DGL relative density in relation with GO concentration. **c** 3DGL density in relation with GO concentration. Samples with 5×5x5 unit cells. **d** Micro-CT scans of cross-sectional view of 3DGL-S (polymer RD of 20%) using four GO concentrations

3.2.1.2 Effect of varying GO concentration and polymer template relative density To assess the effect of GO concentration and polymer template RD on the compressive mechanical properties of 3DGL, four GO concentrations (2, 4, 10, and 15 mg/mL) and two polymer template RDs (7% and 20%) were considered. Figure 11a shows examples of fabricated samples at different GO concentrations for 3DGL-S with 5×5×5 unit cell using a polymer template of 20% RD. Figure 11b and c shows the relationship of GO concentration with 3DGL relative density and density for both tube-ligament and sheet networks; the tube-ligament-network data are taken from [31]. The data in Fig. 11b and c are fitted with a power law that can be used to estimate the expected 3DGL density (or relative density) for a specific GO concentration and gyroid network type.

Figures S6 and S7 (see supplementary document) show the compressive stress–strain curves of 3DGL-S using different GO concentrations for polymer template RDs 7% and 20%, respectively. Figure S8 provides a comparison of the normalized stress–strain curves for both 20 and 7% polymer template RD for the four GO concentrations. Tables S2 and S3 provide the densities, relative densities, and the extracted mechanical properties of 3DGL-S of both 20% and 7% polymer template RD, respectively, for the four GO concentrations. Figure 12a shows that graphene lattices based on 7% polymer template RD have higher graphene relative density as compared to 20% template which is attributed by the higher surface area for the former as evident in Fig. 1b. Also, from Fig. 12, we can notice that the mechanical behavior for 7% template RD yields slightly higher specific stiffness than 20% template RD but significantly higher specific plateau strength and specific toughness. This can be attributed to the good stacking of the graphene micro-sheets after etching the polymer scaffold using a 7% RD polymer template, where the thickness of the polymer sheet is less compared to the one with 20% RD (see Figure S1 in the supplementary document). This produced smaller air gaps inside the graphene coating after thermal etching, as evidenced by micro-CT images in Figs. 6d and S2(b). Moreover, it is observed from Fig. 12 that by increasing the GO concentration at a fixed polymer RD, there is an increase in the 3DGL-S density or relative density due to increase in coating thickness (see Fig. 11d). Also, it can be seen from Fig. 12 that upon increasing the GO concentration at a fixed polymer RD, the 3DGL-S is stiffer due to an increase in 3DGL density or relative density.

3.2.1.3 Deformation behavior Figure 9(b–g) shows deformation patterns taken during testing the samples at two different strain levels ($\varepsilon = 0\%$ and $\varepsilon = 50\%$) for 3DGL-T and 3DGL-S. Figure 9c, e, and g shows that the tube-ligament-network sample undergoes a uniform deformation such that the 3DGL-T collapses in a layer-by-layer mode throughout the compression process, whereas the sheet networks collapse due to strain localization and formation of shear bands that are triggered by manufacturing microstructural defects

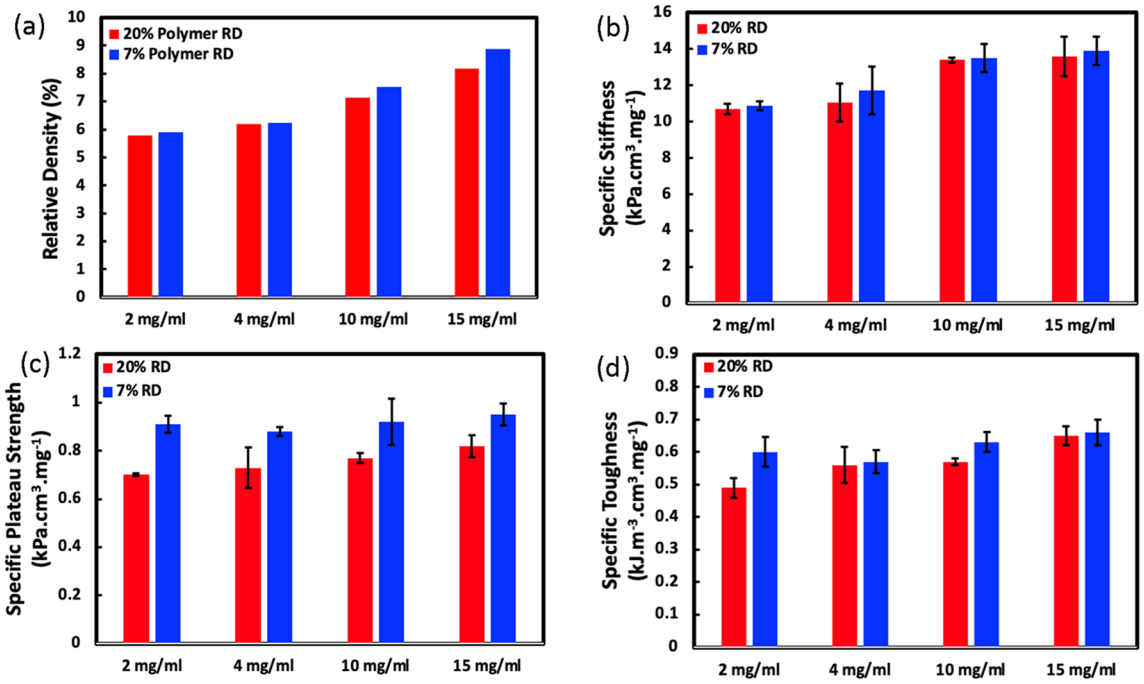

Fig. 12 Effect of GO concentration and polymer template RD on **a** relative density, **b** specific stiffness, **c** specific plateau strength, and **d** specific toughness for 3DGL-S

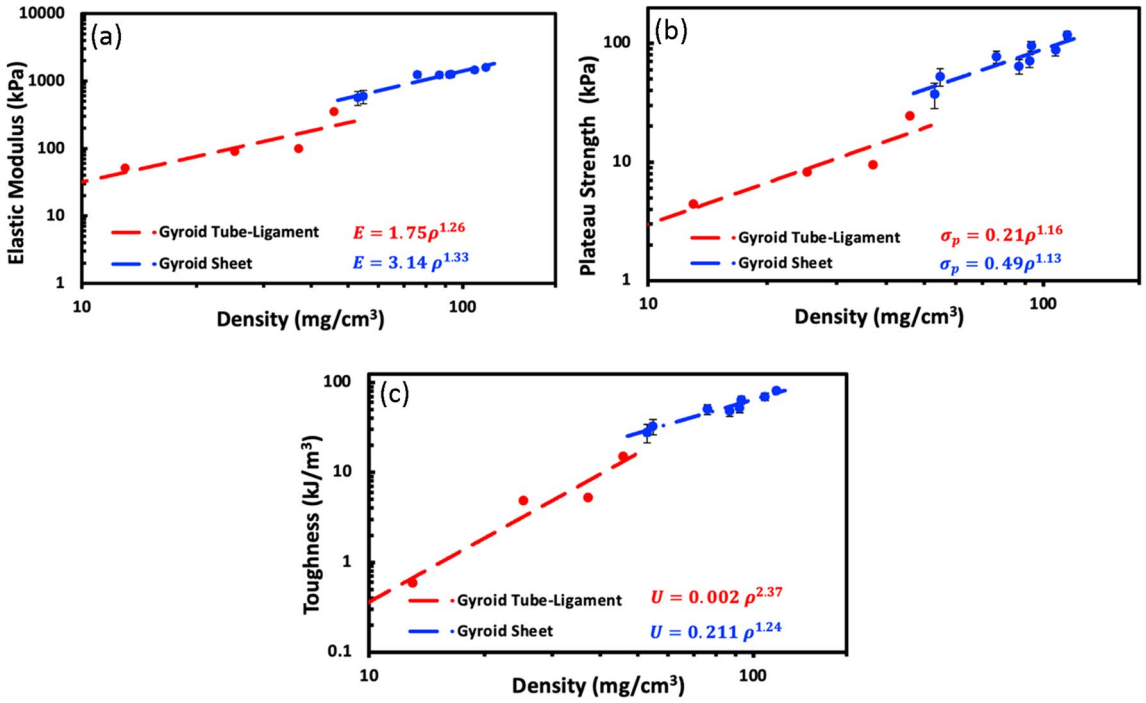

Fig. 13 Experimental results of compressive mechanical properties verses density for the 3DGL-T and 3DGL-S fitted with the Gibson–Ashby scaling power law **a** elastic modulus, **b** plateau strength, and **c** toughness

(see Fig. 9b–f). Also, the deformation patterns of 3DGL-S (5 × 5x5 unit celled) at different GO concentrations can be seen in Figure S9 of the supplementary document. It was observed that all the 3DGL-S fabricated at various GO concentrations have the same deformation pattern. Therefore, this implies that the deformation mechanism is independent of GO concentration, and dependent on the topology network (see Fig. 9).

To evaluate the bending- or stretching-dominated deformation behavior of the current 3DGL, we plot the mechanical properties (elastic modulus, plateau strength, and toughness) as a function of density fitted with the Gibson–Ashby scaling power law $\varphi = C\varphi_s\rho^n$ as shown in Fig. 13. The power law exponent n typically indicates the deformation mode; stretching- or bending-dominated [43]. A value of n≈1 indicates a stretching-dominated mode for the elastic modulus and strength, whereas values of more than 1.5 or 2 depict bending-dominated in the case of elastic modulus and strength, respectively. Furthermore, any value between these two bounds signifies a mixed deformation mode. From Fig. 13, it is observed for the case of 3DGL-S that the exponents n for elastic modulus and strength are 1.33 and 1.13, respectively, indicating a stretching-dominated mode of deformation behavior. Similarly, the stretching-dominated mode of deformation behavior is dominant for 3DGL-T since the Gibson–Ashby power law exponents n for elastic modulus and strength are 1.26 and 1.16, respectively. It is also understood from Fig. 13c that the toughness, which is an indication of lattice's energy absorption, of the 3DGL increases with increasing density, but sheet networks show a higher energy absorption trend with decreasing density compared to tube-ligament networks. The enhanced toughness also indicates better shock-absorption capabilities. Furthermore, Fig. 13 clearly shows that 3DGL-S outperform the stiffness, strength, and toughness of 3DGL-T.

The current 3DGLs exhibited a relatively much smaller scaling exponent, which is a significant improvement over 3D porous graphene aerogels fabricated using hydrothermal reduction process with a scaling exponent of 2.67 [45], indicating bending-dominated behavior. The scaling exponent of the current fabricated 3DGL has a similar value ($n = 1.54$) to the hierarchical micro-architected graphene assemblies fabricated using 3D printing via projection micro-stereolithography [28]. On the other hand, the current 3DGLs are also superior to the previously 3D-printed graphene aerogels that could only behave as bending-dominated structures with a scaling $n = 2.5$ [46]. This is an important finding because the type of deformation mode (i.e., bending, stretching, or mixed mode) dictates the potential application of such lattices.

3.2.1.4 Properties of the graphene lattices base material It is noteworthy that the upper bounds of the elastic modulus E_S and strength σ_s for the rGO coating, which constitute the graphene lattices, can be back-calculated using the upper

bounds in Eqs. (2) and (3), respectively, using a Poisson's ratio of 0.165, a value that is commonly used for rGO base material [47], and the relative density $\overline{\rho}$ of 3DGL measured using the micro-CT scans (see Tables S1, S2, and S3). Also, the density of rGO sheets ρ_S can be calculated using the relative density (or equivalently the graphene volume fraction) values obtained from the micro-CT scans and measured 3DGL density. The calculated values of ρ_S,E_s, and σ_s of rGO base material are listed in Table S4 of the supplementary document for different number of unit cells (or unit cell sizes) and graphene lattice networks (sheet and tube). For 3DGL-S, there is a weaker dependence of the lattice base material properties, especially ρ_S andE_s, on the number/size of the unit cell as compared to that of 3DGL-T. This might indicate that the manufacturing defects in 3DGL-S are less than those in 3DGL-T. Furthermore, the base material properties in 3DGL-S are slightly denser, but stiffer and stronger than that in 3DGL-T.

Moreover, Table S5 in the supplementary document presents the calculated properties of rGO base material (i.e., ρ_S ,E_s, andσ_s) for 3DGL-S with $5\times5\times5$ unit cell for both 7 and 20% polymer RD using different GO concentrations (2, 4, 10, and 15 mg/mL). It can be noticed from Table S5 that ρ_S ,E_s, and σ_s slightly increase with increasing GO concentration with the highest difference at 2 mg/mL concentration. Overall, one can conclude that the base material properties do not change much when using GO concentrations higher than 4 mg/mL. The slight variation in the obtained values could be attributed to the slight variation in base material density and manufacturing defects. Also, it can be noticed from Table S5 that the dependence of the base material properties on the polymer template relative density can generally be neglected.

From the calculated results in Table S5, the average value of the elastic modulus of rGO sheets was calculated to be 30.34 ± 9.40 MPa. The elastic modulus value obtained from the testing is comparable to the measured value of the rGO sheets obtained from the AFM (45.73 ± 5.70 MPa). Furthermore, the average value of rGO base material's density was calculated to be $1{,}116.84\pm168.26$ mg/cm^3, which is relatively close to the reported rGO density (1,500 to 1,900 mg/cm^3) [48].

3.2.1.5 Comparison with data from the literature Figure 14 provides Ashby charts comparing the elastic modulus and strength of 3D graphene cellular materials in literature [9, 27, 28, 30–32, 45, 49–57], and the values reported in this study. For an objective comparison, the specific (i.e., density-normalized) stiffness and specific strength values of 3D graphene structures reported in literature are calculated and presented along with the current results in Table S6 in the supplementary document. It becomes clear that the 3DGLs reported in this study are stiffer than the 3D graphene structures fabricated using other techniques, including CVD [50], hydrothermal process [31, 45, 52, 53], 3D printing process [9], and dip-coating [54, 55]. The current fabricated 3DGLs (both tube and sheet networks) show specific stiffness values ranged from 5.90 to 22.10 kPa.cm^3/mg, and specific strength values varied from 0.49 to 2.12 kPa.cm^3/mg, while 3D graphene structures produced by CVD, hydrothermal process, 3D printing, and dip-coating processes show lower specific stiffness (2.50–7.65 kPa) and comparable specific strength (0.3–3.7 kPa.cm^3/mg). Also, the current 3DGLs are stiffer than the 3D graphene structures fabricated recently through graphene injection into 3D-printed templates (2.27–17.59 kPa) [56] with specific stiffness values of 2.25–17.59 kPa.cm^3/mg that are lower than the specific values of the current 3DGLs-S (11.6–22.10 kPa.cm^3/mg). The current measured values are in good agreement with the values for the graphene structures fabricated using 3D printing [51], and hydrothermal process based on different 3D-printed TPMS topologies reported in our previous work [32]. Although the specific stiffness and specific strength values of the fabricated 3DGLs are lower than the graphene structures fabricated by CVD [27, 30, 49], 3D printing [28], and hydrothermal process using 3D-printed templates [57], there is a margin for improvement by changing several manufacturing parameters, such as increasing the coating material concentration, reducing further the unit cell size, decreasing the template relative density, and using high-quality graphene nanoplatelets instead of rGO. Furthermore, fabrication of the gyroidal graphene lattices using CVD and sacrificial templates will result in improved mechanical properties.

4 Conclusions

In summary, we reported for the first time the synthesis of 3D graphene lattices based on gyroid sheet networks that were fabricated via hydrothermal-assisted dip-coating technique based on additive manufacturing polymer templates. The 3D-printed templates allow the obtained graphene lattices to maintain the complex architecture of the gyroid sheet-based structure, whereas the ligament-based gyroid polymer template resulted in a tubular-ligament hollow graphene networks as previously shown in our previous work [31–33]. The comparison between the sheet/shell and tubular graphene gyroid structures is reported herein for the first time as well. The mechanical properties of 3D graphene gyroidal lattices based on both sheet- and tube-ligament networks were systematically examined by varying the lattice number of unit cell (or unit cell's size), GO concentration, and polymer template relative density. It was found that the mechanical properties of graphene gyroid sheet networks outperformed (almost double) the graphene gyroid tubular-ligament networks. Also, both exhibited

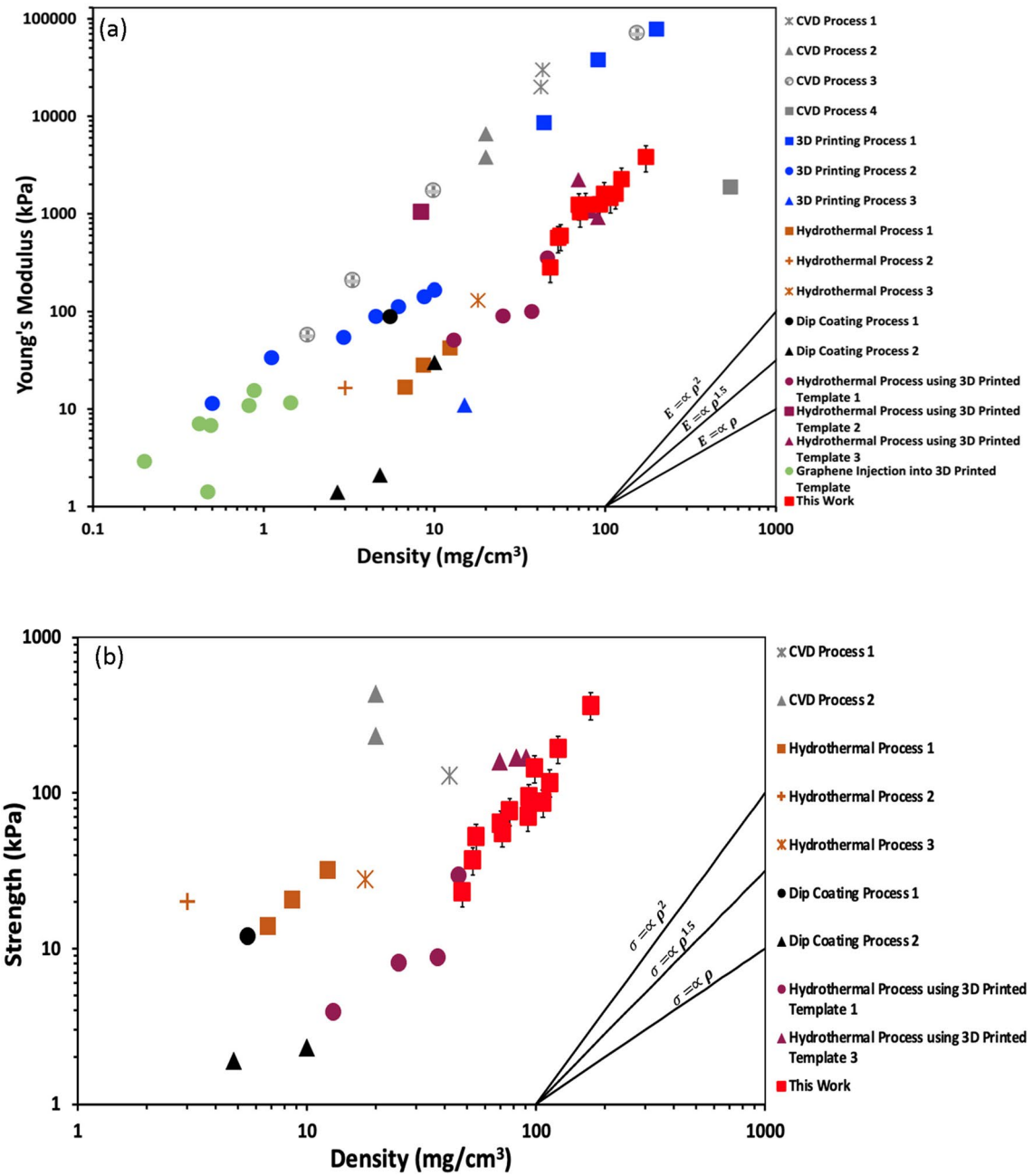

Fig. 14 Ashby charts of the 3DGL compared to the 3D graphene cellular materials in literature including CVD 1 [27], CVD 2 [30], CVD 3 [49], CVD 4 [50], 3D printing process 1 [28], 3D printing process 2 [51], 3D printing process 3 [9], hydrothermal process 1 [45], hydrothermal process 2 [52], hydrothermal process 3 [53], dip-coating process 1 [54], dip-coating process 2 [55], hydrothermal process using 3D-printed template 1 [31], hydrothermal process using 3D-printed template 2 [57], hydrothermal process using 3D-printed template 3 [32], and graphene injection into 3D-printed template process [56] **a** Young's modulus and **b** compressive strength

stretching-dominated behavior in the elastic and plastic regions, which is beneficial for obtaining stiffer and stronger graphene architected structures as compared to 3D porous graphene aerogels that are mainly bending-dominated. Furthermore, the graphene sheet networks showed a better energy absorption trend with decreasing graphene lattice relative density. It was shown that decreasing unit cell size, increasing GO concentration, and decreasing polymer template relative density, generally, increases the mechanical properties of the gyroid graphene lattices, allowing for potential future enhancements in mechanical properties by adjusting these parameters. However, decreasing the unit cell size significantly increased the mechanical properties in comparison with increasing GO concentration or reducing polymer template relative density. Thus, further decrease

in the template's unit cell size, which is limited by the adapted 3D printing technique, is an effective way for enhancing the mechanical properties of the current gyroidal graphene structures. Furthermore, polymer templates with smaller relative density resulted in better mechanical properties mainly due to better stacking of graphene micro-sheets and reduced defects.

Using theoretical stiffness and strength upper bounds, the density, stiffness, and strength of the rGO base material that constitutes the current fabricated gyroidal graphene lattices were calculated and found to slightly vary with GO concentration and unit cell size. This variation is mainly attributed to manufacturing defects. Close agreement between the calculated rGO density ($1{,}116.84 \pm 168.26$ mg/cm^3) and those from the literature is found. Furthermore, fair agreement between the calculated rGO stiffness (30.34 ± 9.40 MPa) and measured stiffness (45.73 MPa) by Atomic Force Microscope is obtained. It is also concluded that the density-normalized stiffness and strength of the current sheet-based gyroidal graphene structures are higher than those of many graphene cellular structures that are produced by various fabrication techniques in the literature.

The fabrication of gyroidal, and generally TPMS, graphene cellular structures paves the way for multi-functional bulk materials for many applications, including energy storage, thermal management, catalytic support, pressure sensors, bio-scaffolds, and electromagnetic shielding/cloaking.

Supplementary Information The online version contains supplementary material available at https://doi.org/10.1007/s41127-023-00066-2.

Acknowledgements The authors acknowledge the financial support provided by Khalifa University under Award No. RCII-2019-003. The open-access fees of this paper were supported by Abu Dhabi National Oil Company (ADNOC), Emirates NBD, Sharjah Electricity Water and Gas Authority (SEWA), and Dubai Electricity and Water Authority (DEWA) R&D Center as the sponsors of the 3rd Forum for Women in Research: Women Empowerment for Global Impact at University of Sharjah. The authors also acknowledge the help of Pradeep George and Wesley Cantwell from the KU Advanced Research and Innovation Center for generating the micro-CT images. The authors also acknowledge the help of Cyril Aubry for performing the AFM analysis.

Author contributions Somayya Taher contributed to writing—original draft preparation, methodology, formal analysis, investigation, and visualization.Juveiriah Ashraf was involved in formal analysis, investigation, visualization, and methodology.Kin Liao contributed to methodology, writing—review and editing, and supervision.Rashid Abu Al-Rub was involved in conceptualization, methodology, writing—review and editing, supervision, project administration, and funding acquisition.

Availability of data and materials The raw data required to reproduce these findings are available from the corresponding author (RK Abu Al-Rub) based on a reasonable request.

Declarations

Conflict of interest The authors declare there are no conflicts to declare.

References

1. Geim AK, Novoselov KS (2010) The rise of graphene. Nanosci Technol Collection Rev Nat J World Sci, p 11–29
2. Naguib M, Mochalin VN, Barsoum MW, Gogotsi Y (2014) 25th Anniversary article: MXenes: a new family of two-dimensional materials. Adv Mater 26:992–1005
3. Soldano C, Mahmood A, Dujardin E (2010) Production, properties and potential of graphene. Carbon 48:2127–2150
4. Choi W, Lahiri I, Seelaboyina R, Kang YS (2010) Synthesis of graphene and its applications: a review. Crit Rev Solid State Mater Sci 35:52–71
5. Ma R, Zhou Y, Bi H, Yang M, Wang J, Liu Q et al (2020) Multi-dimensional graphene structures and beyond: unique properties, syntheses and applications. Prog Mater Sci 113:100665
6. Sun Z, Fang S, Hu YH (2020) 3D graphene materials: from understanding to design and synthesis control. Chem Rev 120:10336–10453
7. Chen Z, Xu C, Ma C, Ren W, Cheng HM (2013) Lightweight and flexible graphene foam composites for high-performance electromagnetic interference shielding. Adv Mater 25:1296–1300
8. Worsley MA, Pauzauskie PJ, Olson TY, Biener J, Satcher JH Jr, Baumann TF (2010) Synthesis of graphene aerogel with high electrical conductivity. J Am Chem Soc 132:14067–14069
9. Sha J, Li Y, Villegas Salvatierra R, Wang T, Dong P, Ji Y et al (2017) Three-dimensional printed graphene foams. Acs. NANO 11:6860–6867
10. Seyedsalehi A, Daneshmandi L, Barajaa M, Riordan J, Laurencin CT (2020) Fabrication and characterization of mechanically competent 3D printed polycaprolactone-reduced graphene oxide scaffolds. Sci Rep 10:22210
11. Wang Y-Y, Sun W-J, Yan D-X, Dai K, Li Z-M (2021) Ultralight carbon nanotube/graphene/polyimide foam with heterogeneous interfaces for efficient electromagnetic interference shielding and electromagnetic wave absorption. Carbon 176:118–125
12. Zhu C, Han TY-J, Duoss EB, Golobic AM, Kuntz JD, Spadaccini CM, et al. (2015) Highly compressible 3D periodic graphene aerogel microlattices. Nat Commun 6:1–8
13. Du J, Fu G, Xu X, Elshahawy AM, Guan C (2023) 3D printed graphene-based metamaterials: guesting multi-functionality in one gain. Small, pp 2207833
14. Yang R, Zhou J, Yang C, Qiu L, Cheng H (2020) Recent progress in 3D printing of 2D material-based macrostructures. Adv Mater Technol 5:1901066
15. Al-Ketan O, Abu Al-Rub RK (2019) Multifunctional mechanical metamaterials based on triply periodic minimal surface lattices. Adv Eng Mater 21:1900524
16. Al-Ketan O, Pelanconi M, Ortona A, Abu Al-Rub RK (2019) Additive manufacturing of architected catalytic ceramic substrates based on triply periodic minimal surfaces. J Am Ceram Soc 102:6176–6193

17. Sreedhar N, Thomas N, Al-Ketan O, Rowshan R, Hernandez H, Abu Al-Rub RK et al (2018) 3D printed feed spacers based on triply periodic minimal surfaces for flux enhancement and biofouling mitigation in RO and UF. Desalination 425:12–21
18. Kapfer SC, Hyde ST, Mecke K, Arns CH, Schröder-Turk GE (2011) Minimal surface scaffold designs for tissue engineering. Biomaterials 32:6875–6882
19. Yoo DJ (2011) Porous scaffold design using the distance field and triply periodic minimal surface models. Biomaterials 32:7741–7754
20. Qureshi ZA, Al Omari SAB, Elnajjar E, Mahmoud F, Al-Ketan O, Abu Al-Rub R (2021) Thermal characterization of 3D-Printed lattices based on triply periodic minimal surfaces embedded with organic phase change material. Case Stud Thermal Eng, 101315
21. Alteneiji M, Ali MIH, Khan KA, Abu Al-Rub RK (2022) Heat transfer effectiveness characteristics maps for additively manufactured TPMS compact heat exchangers. Energy Storage Saving 1:153–161
22. Al-Ketan O, Rezgui R, Rowshan R, Du H, Fang NX, Al-Ketan O et al (2018) Microarchitected stretching-dominated mechanical metamaterials with minimal surface topologies. Adv Eng Mater 20:1800029
23. Schwarz HA (1972) Gesammelte mathematische abhandlungen. Am Math Soc
24. Schoen AH (1970) Infinite periodic minimal surfaces without self-intersections. National Aeronautics and Space Administration
25. Khaderi S, Deshpande V, Fleck N (2014) The stiffness and strength of the gyroid lattice. Int J Solids Struct 51:3866–3877
26. Al-Ketan O, Rowshan R, Abu Al-Rub RK (2018) Topology-mechanical property relationship of 3D printed strut, skeletal, and sheet based periodic metallic cellular materials. Addit Manuf 19:167–183
27. Garcia AE, Wang CS, Sanderson RN, McDevitt KM, Zhang Y, Valdevit L et al (2019) Scalable synthesis of gyroid-inspired free-standing three-dimensional graphene architectures. Nanoscale Advances 1:3870–3882
28. Hensleigh RM, Cui H, Oakdale JS, Jianchao CY, Campbell PG, Duoss EB et al (2018) Additive manufacturing of complex micro-architected graphene aerogels. Mater Horiz 5:1035–1041
29. Cebo T, Aria AI, Dolan JA, Weatherup RS, Nakanishi K, Kidambi PR et al (2017) Chemical vapour deposition of freestanding sub-60 nm graphene gyroids. Appl Phys Lett 111:253103
30. Kashani H, Ito Y, Han J, Liu P, Chen M (2019) Extraordinary tensile strength and ductility of scalable nanoporous graphene. Sci Adv 5:eaat6951
31. Ashraf JM, Fu J, Liao K, Chan V, Abu Al-Rub RK (2021) Scalable synthesis, characterization and testing of 3D architected gyroid graphene lattices from additively manufactured templates. J Micromech Mol Phys, pp 1–12
32. Ashraf JM, Taher SE, Lee D-W, Liao K, Abu Al-Rub RK (2022) On the computational modeling, additive manufacturing, and testing of tube-networks TPMS-based graphene lattices and characterizing their multifunctional properties. APL Mater 10:121107
33. Fu J, Taher SE, Abu Al-Rub RK, Zhang T, Chan V, Liao K (2022) Engineering 3D-architected gyroid MXene scaffolds for ultrasensitive micromechanical sensing. Adv Eng Mater, pp 2101388
34. Al-Ketan O, Abu Al-Rub RK (2021) MSLattice: A free software for generating uniform and graded lattices based on triply periodic minimal surfaces. Mater Des Process Commun 3:e205
35. Lee C, Wei X, Kysar JW, Hone J (2008) Measurement of the elastic properties and intrinsic strength of monolayer graphene. Science 321:385–388
36. Malina E (2011) Mechanical behavior of atomically thin graphene sheets using atomic force microscopy nanoindentation. University of Vermont, USA
37. Crook C, Bauer J, Guell Izard A, Santos de Oliveira C, Martins de Souza e Silva J, Berger JB, et al. (2020) Plate-nanolattices at the theoretical limit of stiffness and strength. Nat Commun 11:1–11
38. Yoon M, Howe J, Tibbetts G, Eres G, Zhang Z (2007) Polygonization and anomalous graphene interlayer spacing of multi-walled carbon nanofibers. Phys Rev B 75:165402
39. Huang H-H, De Silva KKH, Kumara G, Yoshimura M (2018) Structural evolution of hydrothermally derived reduced graphene oxide. Sci Rep 8:1–9
40. Muhammed Shafi P, Chandra BA (2015) Impact of crystalline defects and size on X-ray line broadening: a phenomenological approach for tetragonal SnO2 nanocrystals. AIP Adv 5:057137
41. Ren P-G, Yan D-X, Ji X, Chen T, Li Z-M (2010) Temperature dependence of graphene oxide reduced by hydrazine hydrate. Nanotechnology 22:055705
42. Muzyka R, Drewniak S, Pustelny T, Chrubasik M, Gryglewicz G (2018) Characterization of graphite oxide and reduced graphene oxide obtained from different graphite precursors and oxidized by different methods using Raman spectroscopy. Materials 11:1050
43. Gibson L, Ashby M (1999) Cellular solids: structure and properties. Cambridge Univ, Pr
44. Zheng X, Lee H, Weisgraber TH, Shusteff M, DeOtte J, Duoss EB et al (2014) Ultralight, ultrastiff mechanical metamaterials. Science 344:1373–1377
45. Li Y, Chen J, Huang L, Li C, Hong JD, Shi G (2014) Highly compressible macroporous graphene monoliths via an improved hydrothermal process. Adv Mater 26:4789–4793
46. Qin Z, Jung GS, Kang MJ, Buehler MJ (2017) The mechanics and design of a lightweight three-dimensional graphene assembly. Sci Adv 3:e1601536
47. Suk JW, Piner RD, An J, Ruoff RS (2010) Mechanical properties of monolayer graphene oxide. ACS Nano 4:6557–6564
48. Torrisi L, Cutroneo M, Torrisi A, Silipigni L (2022) Measurements on five characterizing properties of graphene oxide and reduced graphene oxide foils. physica status solidi (a) 219:2100628
49. Bi H, Chen IW, Lin T, Huang F (2015) A new tubular graphene form of a tetrahedrally connected cellular structure. Adv Mater 27:5943–5949
50. Reddy SK, Ferry DB, Misra A (2014) Highly compressible behavior of polymer mediated three-dimensional network of graphene foam. RSC Adv 4:50074–50080
51. Zhang Q, Zhang F, Medarametla SP, Li H, Zhou C, Lin D (2016) 3D printing of graphene aerogels. Small 12:1702–1708
52. Hu H, Zhao Z, Wan W, Gogotsi Y, Qiu J (2013) Ultralight and highly compressible graphene aerogels. Adv Mater 25:2219–2223
53. Chen W, Yan L (2011) In situ self-assembly of mild chemical reduction graphene for three-dimensional architectures. Nanoscale 3:3132–3137
54. Samad YA, Li Y, Alhassan SM, Liao K (2015) Novel graphene foam composite with adjustable sensitivity for sensor applications. ACS Appl Mater Interfaces 7:9195–9202
55. Du X, Liu H-Y, Mai Y-W (2016) Ultrafast synthesis of multifunctional N-doped graphene foam in an ethanol flame. ACS Nano 10:453–462
56. Zhou J, Wu X, Chen Y, Yang C, Yang R, Tan J et al (2022) 3D printed template-directed assembly of multiscale graphene structures. Adv Func Mater 32:2105879
57. Zhang Q, Zhang F, Xu X, Zhou C, Lin D (2018) Three-dimensional printing hollow polymer template-mediated graphene lattices with tailorable architectures and multifunctional properties. ACS Nano 12:1096–1106